European Journal of Biophysics
2021; 9(1): 13-23
http://www.sciencepublishinggroup.com/j/ejb
doi: 10.11648/j.ejb.20210901.13
ISSN: 2329-1745 (Print); ISSN: 2329-1737 (Online)

Crystal Structure of Peptidyl-tRNA Hydrolase from *Acinetobacter baumannii* at 1.00 Å Resolution

Vijayan Viswanathan, Pradeep Sharma, Prashant Kumar Singh, Punit Kaur, Sujata Sharma, Tej Pal Singh*

Department of Biophysics, All India Institute of Medical Sciences, New Delhi, India

Email address:
tpsingh.aiims@gmail.com (T. P. Singh)

*Corresponding author

To cite this article:
Vijayan Viswanathan, Pradeep Sharma, Prashant Kumar Singh, Punit Kaur, Sujata Sharma, Tej Pal Singh. Crystal Structure of Peptidyl-tRNA Hydrolase from *Acinetobacter baumannii* at 1.00 Å Resolution. *European Journal of Biophysics*. Vol. 9, No. 1, 2021, pp. 13-23.
doi: 10.11648/j.ejb.20210901.13

Received: February 20, 2021; **Accepted**: March 8, 2021; **Published**: March 13, 2021

Abstract: The essential process of protein biosynthesis in the cell often gets stalled due to the premature abortion of the translation process and generates a byproduct of peptidyl-tRNA molecules. This defect is corrected by peptidyl-tRNA hydrolase (Pth) by hydrolyzing peptidyl-tRNA to yield tRNA and peptides. In order to understand the mechanism of catalytic action and detailed stereochemical features of the substrate binding site, the structure of *Pth* has been determined at 1.00 Å resolution. The *Pth* enzyme from *Acinetobacter baumannii* (*Ab*Pth) was cloned, expressed, purified and crystallized. The structure was refined to R_{cryst} and R_{free} values of 0.145 and 0.157 respectively. The electron densities were observed for many hydrogen atoms in the structure. In *Ab*Pth, the residues, Asn12, His22, Asn70, Asp95 and Asn116 are involved in the catalytic process. The structure determination revealed that His22 $N^{\delta1}$ forms a hydrogen bond with Asp95 $O^{\delta2}$ while His22 $N^{\varepsilon2}$ is hydrogen bonded to Asn116 $N^{\delta2}$. In this case, the side chain of Asn116 adopts a conformation with χ value of 65°. Upon ligand binding, Asn116 adopts a different conformation with χ value of -70^0. In the present structure, the conformation of Tyr68 is observed in the disallowed region of Ramachandran's plot with φ, ψ values of 80^0, 150^0. However, it is observed that Tyr68 adopts both disallowed and allowed conformations in Pth enzymes indicating a structural flexibility. The structure determination also revealed multiple conformations of the side chains of a number of amino acid residues.

Keywords: Peptidyl-tRNA Hydrolase, Crystal Structure, Atomic Resolution, Catalytic Site, Protonation

1. Introduction

Petidyl-tRNA hydrolase (Pth, EC 3.1.1.29) catalyzes the hydrolysis of peptidyl-tRNA molecules for separating the peptide and tRNA components. The peptidyl-tRNA molecules are produced due to a prematurely terminated translation process during protein biosynthesis [1-4]. This undesirable byproduct results in the loss of tRNA and amino acids which adversely affects the process of protein biosynthesis eventually leading to cell death [5-8]. The stalled process of protein biosynthesis in the cell is restored by Pth enzyme which is an esterase and cleaves the peptidyl-tRNA molecule at the ester bond between tRNA and peptide component. It ensures the continuous supply of required raw material of tRNA and amino acids so that the process of protein biosynthesis continues without disruptions. In view of this, the role of Pth enzyme is essential in the regulation of protein biosynthesis in the cell.

Initially Pth was identified in *Escherichia coli* [9-11]. Later on, it was reported in yeast [12-15] as well as in several other bacteria [16-21]. There is more than one type of Pth enzymes in different living organisms. In the beginning, it was reported as Pth1 in bacteria and eukaryotic cells [14, 22-23] and Pth2 in archaea and other eukaryotes [15, 24, 25]. In addition to Pth1 and Pth2, Pth-like enzymes are also present in eukaryotes [15, 25, 26]. Pth1 is an essential enzyme in bacteria for maintaining the translation function of ribosome while it is not absolutely necessary in eukaryotes [14-15, 27]. Furthermore, Pth1 is neither chemically nor structurally identical to Pth2 [28]. The structural differences between Pth1 and Pth2 clearly indicate that the inhibitors of Pth1 will

be harmful mainly to bacteria with limited effect on the humans. Thus, the design of inhibitors of Pth1 will be useful for drug design against bacterial infections. Since only Pth1 will be discussed in the present study, it will be referred to hereafter as Pth.

The crystal structures of Pth enzyme from nearly a dozen of bacteria including *Acinetobacter baumannii* (*Ab*Pth) [28], *Pseudomonas aeruginosa* (*Pa*Pth) [29], *Escherichia coli* (*Ec*Pth) [11], *Salmonella typhimurium* (*St*Pth) [30], *Burkholderia structome* (*Bt*Pth) [31], *Vibrio cholerae* (*Vc*Pth) [32], *Francisella tularensis* (*Ft*Pth) [33], *Mycobacterium tuberculosis* (*Mt*Pth) [17], *Mycobacterium smegmatis* (*Ms*Pth) [34], *Staphylococcus aureus* (*Sa*Pth) [35], *Thermus thermophilus* (*Tt*Pth) [36], *Streptococcus pyogenes* (*Sp*Pth) [37] are known. First seven structures of Pth from the above list are from Gram-negative bacteria while the last four structures belong to Gram-positive bacteria. Most of these structures have been determined at moderate resolutions except the structures of *Ec*Pth [11], the complex of *Ab*Pth with cyatarabine [38] and *Tt*Pth [36], which were determined at 1.20 Å, 1.10 Å and 1.00 Å respectively. Here, we report a structure of *Ab*Pth at 1.00 Å resolution giving several new insights.

2. Material and Methods

2.1. Gene Cloning Expression, Purification and Crystallization

The cloning, expression and purification of *Ab*Pth were carried out as described previously [19, 28]. The genomic DNA from *Acinetobacter baumannii* was isolated and *Pth* gene was amplified using forward and reverse primers (Pthf: 5-GGAATTCCATATGTCAAATATTT CGCTAATTG-3′) and (Pthr: 5-CCGCTCGAGTTAAGCTGGTTTATACGCATT-3′) respectively. After further steps, the construct obtained with pET 28a was transformed in *E. coli* (Bl21 DE3) cells for expression of *Ab*Pth. After additional steps, a single fresh colony obtained after transformation in *E. coli* (BL21 DE3) cells was inoculated in LB medium supplemented with 50 mg/ml kanamycin and grown at 37°C. Cells were harvested by centrifugation at 6000g for 5min at 4°C. Approximately 5g of the wet pellet was suspended in 15-20ml of 50mM Tris HCl buffer containing 150 mM NaCl, pH 8.0 (lysis buffer). After sonication, the ruptured cells were centrifuged at 13000g for 30min at 4°C. The cleared lysate was loaded on a Ni-NTA Super-flow column (Qiagen, Germantown, MD, USA) which was pre-equilibrated in lysis buffer. The protein samples were further purified using stepwise washing with 30mM imidazole in lysis buffer followed by 300mM imidazole in lysis buffer. The protein samples of each fraction were evaluated on 11% sodium dodecyl sulfate - polyacrylamide gel electrophoresis (SDS-PAGE). The fractions corresponding to molecular mass of approximately 20kDa were pooled. The imidazole was removed by dialysis in lysis buffer and the sample was concentrated using centricon with molecular mass of 3 kDa cut-off (Millipore, Middlesex Tumpike, MA, USA). The concentrated protein was further purified using Fast protein liquid chromatography (Bio-rad Laboratories, Hercules, CA, USA) using superdex G75 column in buffer containing 20mM Tris. HCl, 50 mM NaCl, 1mM Ethylene diamine tetra acetic acid (EDTA), and 5mM of 2-mercaptoethanol, pH7.5. The eluted protein samples were again concentrated using a centric on ultrafiltration with a molecular mass cut off of 3 kDa (Millipore, Middlesex Tumpike, MA, USA). The purity of protein samples was confirmed using SDS-PAGE.

The purified protein samples were dissolved in 0.3M HEPES buffer, pH7.0 at a concentration of 15mg/ml which were kept for crystallization using hanging drop vapour-diffusion method at 298K using 24 well linbro crystallization plates. Crystals were obtained by equilibrating 10µl protein drop against a reservoir solution containing 12% PEG-1500 in 0.3M HEPES buffer at pH 7.0. Crystals grew in two weeks to approximate dimensions of $0.4 \times 0.4 \times 0.2$ mm^3.

Table 1. *Data collection and refinement statistics of Peptidyl-tRNA hydrolase from Acinetobacter baumannii at 1.00 Å resolution (values in parentheses are for the highest resolution shell).*

Data collection	
Resolution range (Å)	33.13 – 1.00
Beam line (ESRF, France, Italy)	ID23-1
Wavelength (Å)	0.97
Space group	P $2_1 2_1 2_1$
Unit-cell parameters (Å)	a = 33.99, b = 66.26, c = 76.19
Number of molecules in the asymmetric unit	1
V_m (Å^3/Da)	2.0
Solvent Content (%)	40.0
Total number of reflections	761316
Number of unique reflections	79893
Overall completeness (%)	97.3 (98.8)
R_{merge}(%)	9.3 (79.8)
R_{pim} (%)	3.8 (26.3)
I / σ(I)	11.1 (2.4)
CC(1/2)(%)	99.6 (74.3)
Redundancy	9.5 (8.5)
Refinement statistics	
R_{cryst} (%)	14.5
R_{free} (3% data) (%)	15.7
Assigned residues	-2 to 0 and 1 to 193
Number of protein atoms	1536
Number of water molecules	239
R. m. s. deviations	
Bond length (Å)	0.018
Bond angles (^{0})	2.093
Dihedral angles (^{0})	12.565
Mean B-factor (Å^2)	
Wilson B-factor	7.3
Main chain atoms	12.2
Side chains and water molecules	16.7
Overall	17.0
Ramachandran plot statistics	
Residues in the most favored region (%)	93.0
Residues in the additional allowed region (%)	5.7
Residues in the generously allowed region (%)	0.6
Residues in the disallowed region (%) [Tyr68]	0.6
PDB ID	7CSN

Data collection and processing

Crystals of *Ab*Pth were stabilized by transferring them to reservoir solution to which 25% glycerol was added. Crystals were mounted in a nylon loop and flash frozen for data collection at 100K. X-ray diffraction intensity data were recorded on MAR-225 CCD detector (Marresearch, Norderstedt, Germany) using beamline, BM14 at the European Synchrotron Radiation Facility (ESRF), Grenoble, France. A total of 400 images were collected using an oscillation range of 1° with an exposure time of 4s per image with a wavelength of 0.98Å. It gave a complete data to 0.95Å resolution. The data were processed using XDS [39]**.** Crystals belonged to orthorhombic space group $P2_12_12_1$ with unit cell dimensions of a = 33.99Å, b = 66.26Å, c = 76.19Å. The Matthews constant V_m [40] was 2.0 $Å^3$/Da which corresponded to a solvent content of 39%. The data were processed and scaled using XDS and XSCALE [39] from XDS package. The summary of the data collection, processing and refinement is given in Table 1.

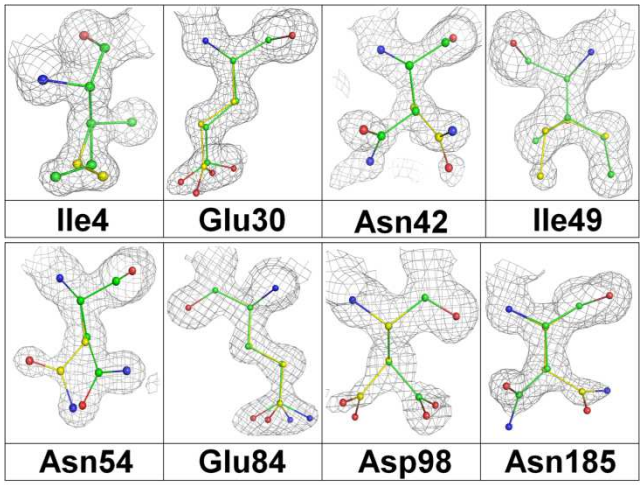

Figure 1. *The initial (2Fo - Fc) electron density map at 1.5σ for selected residues indicating dual conformations. These maps were drawn using COOT [47].*

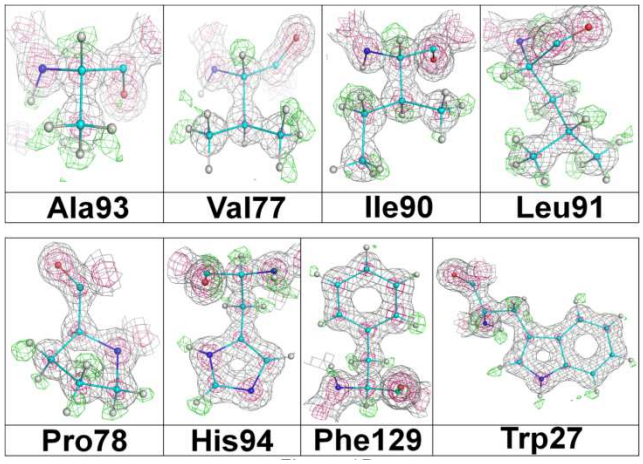

Figure 2. *The omit (Fo - Fc) electron density map at 2σ (green) is superimposed on (2Fo - Fc) electron density maps contoured at 1.5 σ (black) and 5 σ (pink) indicating the positions of hydrogen atoms and accurate positions of non-hydrogen atoms for selected residues.*

2.2. Structure Determination and Refinement

The structure was refined using REFMAC5.8.0.2 [41] using the coordinates of a previously determined structure of *Ab*Pth which has similar unit cell dimensions (PDB ID Code: 4JX9). Initially, the structure was refined for 25 cycles. The electron density maps were calculated using (2Fo - Fc) and (Fo - Fc) coefficients. The model was adjusted manually using COOT [42]. This was followed by another 10 rounds of refinements. When the R_{cryst}/R_{free} factors dropped to 0.21/ 0.24, a difference Fourier map (Fo - Fc) was computed from which positions of 239 water oxygen atoms were determined. After further adjudgments of the protein chain as well as by including the coordinates of 239 water oxygen atoms, the values of R_{cryst} and R_{free} factors dropped to 0.157 and 0.177 respectively. The difference (Fo - Fc) Fourier map calculated at this stage showed electron densities for multiple conformations for a number of residues (Figure 1). With these inputs, the structure of *Ab*Pth was further refined for 15 cycles including anisotropic refinement for non-hydrogen atoms. The refinement finally converged to values of 0.145 and 0.157 for R_{cryst} and R_{free} factors respectively. After completing the refinement, the final (2Fo-Fc) and (Fo-Fc) Fourier maps were computed. An examination of the (Fo-Fc) map indicated electron densities for a number of hydrogen atoms at 2σ cut offs (Figure 2). The validation of structure was carried out using program PROCHECK [43]. The final refined model of *Ab*Pth consisted of 1496 protein atoms and 239 water oxygen atoms. The data quality and final refinement statistics are listed in Table 1. The coordinates and structure factors have been deposited in the protein data bank with accession code of 7CSN.

3. Results and Discussion

3.1. Structure Analysis

The structure of *Ab*Pth consists of 196 residues from the amino acid sequence of Gly-2 - Ser-1 - His- 0 - Met1 to Ala193 (Figure 3) in which the first three residues are from the signal peptide. The structure has been determined at 1.00 Å resolution and refined to values of 0.145 and 0.157 for R_{cryst} and R_{free} factors respectively. In this structure, 93.1% residues are present in the most favored regions of the Ramachandran's φ, ψ map[44] (Figure 4). There are 5.7% residues in the additionally allowed regions and Met1 (0.6%) is present in the generously allowed region while 0.6% (Tyr68) is observed in the disallowed region [43] (Figure 4). It may be mentioned here that Tyr68 is not strictly conserved at position 68 as out of the known structures of Pth enzyme from twelve different bacteria, six of them [17, 28-29, 31, 33, 36] have Tyr68 while four of them [11, 30, 32, 37] have Phe68. The remaining two have Ser68 [34] and Met68 [35] respectively. Both Ser68 and Met68 are observed in the allowed regions. Out of the remaining ten, seven of them [11, 28, 30-31, 33, 36-37] were reported with disallowed conformations for residues at position 68 (Table 2) while in three of them [17, 29, 32], the residues at position 68 were

present in the allowed regions of the Ramachandran's φ, ψ map [44] (Table 2). This shows that both conformations of Tyr68/Phe68 can occur in the structures of Pth indicating a structural flexibility of Tyr68/Phe68. This means that the conformations of Tyr68/Phe68 are more commonly observed in the disallowed regions. A comparison of electron densities of Tyr68 for its conformations in the disallowed (present structure) and allowed [29] regions is shown in figure 6A.

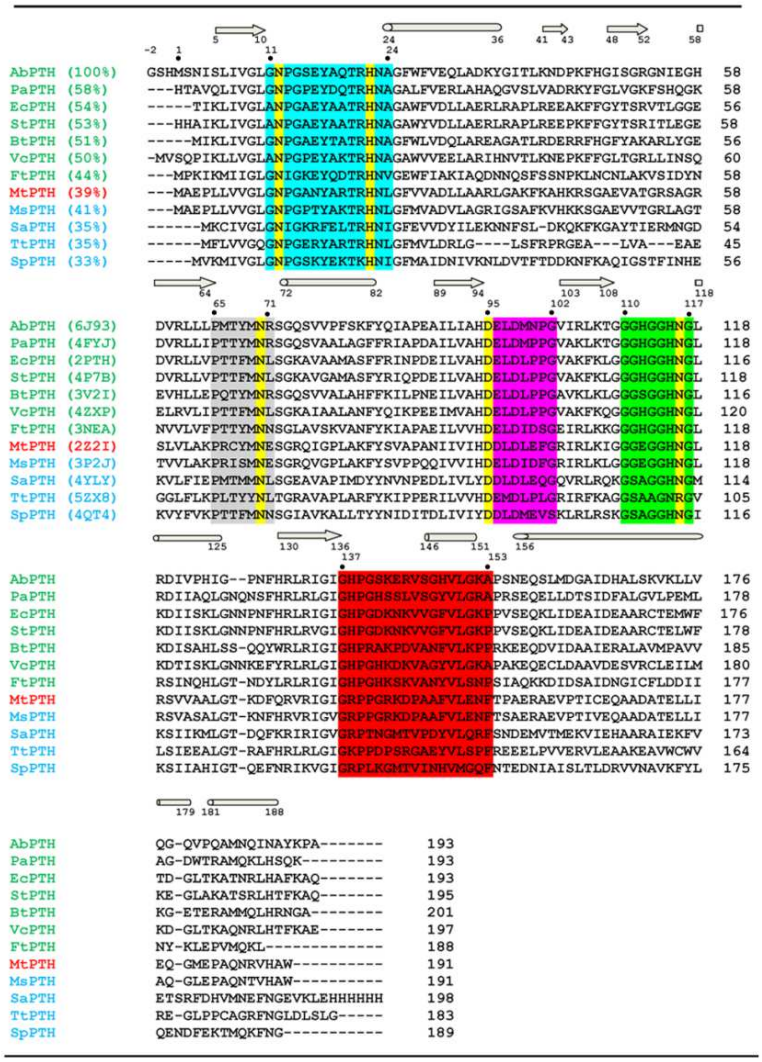

Figure 3. *Comparison of amino acid sequences of Pth enzymes from those bacteria whose crystal structures are known including AbPth, PaPth, EcPth, StPth, BtPth, VcPth, FtPth, MtPth, MsPth, SaPth, TtPth, and SpPth. The top seven sequences are for Pth enzymes from Gram negative bacteria while the bottom four are from Gram positive bacteria. The sequence of MtPth is also given. In case of BtPth, an extra segment of 10 amino acid residues, DMIPESARAG from 140 to 149 has been excluded from figure for clarity. Five loops, Sandwich (cyan), Base' (grey), Gate (magenta), Base (green) and Lid (red) are indicated. The active site residues are highlighted in yellow. The secondary structure elements such as α-helices and β-strands are indicated at the top of sequences.*

Table 2. *Characteristic distances between the active sit loops in Pth enzymes from different bacterial. The first seven proteins are from Gram-negative bacteria while the last four are from Gram-positive bacteria. MtPTH does not belong to either of them. The torsion angles (Φ, Ψ) of Tyr68 are listed in the last column.*

Protein Name	PDB - ID	Distance (Å) (Gly113C$^{\alpha}$- Asp98O$^{\delta2}$)	Distance (Å) (Gly113C$^{\alpha}$- Ser146C$^{\alpha}$)	Distance (Å) (Gly113C$^{\alpha}$- His22C$^{\varepsilon1}$)	Torsion Angles of Tyr68 (°)	
					Φ	Ψ
*Ab*PTH	7CSN	7.85	14.91	10.63	80	150
*Pa*PTH	4FYJ	6.08	13.25	10.09	-67	139
*Ec*PTH	2PTH	6.66	14.93	10.84	93	148
*St*PTH	4P7B	5.74	14.37	10.24	78	151
*Bt*PTH	3V2I	4.97	13.22	10.35	75	152
*Vc*PTH	4ZXP	6.60	13.54	10.37	-54	148
*Ft*PTH	3NEA	6.84	15.02	11.60	78	153
*Mt*PTH	2Z2I	3.33	11.41	9.41	-73	154
*Ms*PTH	3P2J	3.98	11.12	9.70	-60	141
*Sa*PTH	4YLY	6.56	15.29	11.17	-91	177
*Tt*PTH	5ZX8	6.81	15.32	11.40	83	151
*Sp*PTH	4QT4	8.78	13.02	10.38	86	145

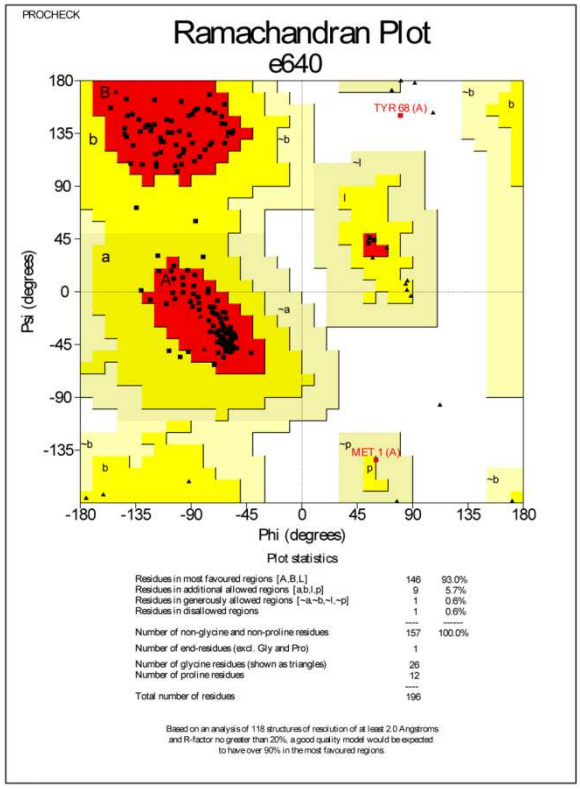

Figure 4. *Ramachandran's φ, ψ plot[44] as drawn using PROCHECK[43].*

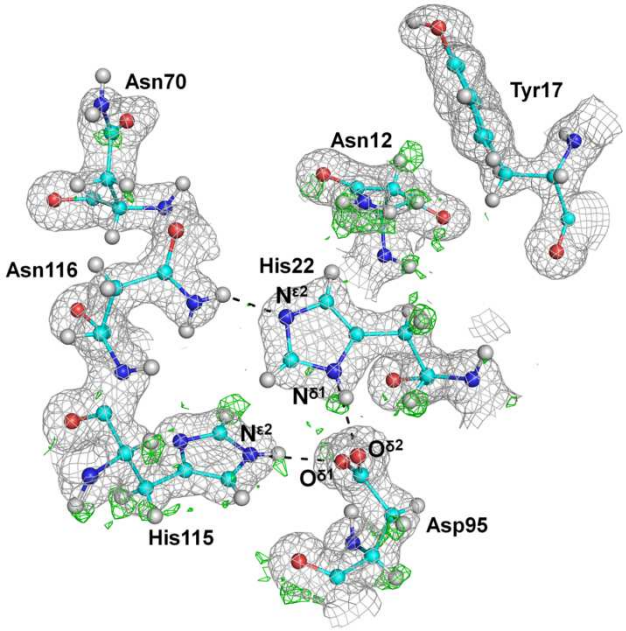

Figure 5. *The final (2Fo - Fc) electron density map at 1.5 σ cut off (black) for residues in the catalytic site. The (Fo - Fc) electron density at 2.0 σ cut off (green) calculated at the end of the refinement. The electron density for hydrogen atoms is observed at His22 $N^{\delta 1}$ and His115 $N^{\varepsilon 2}$.*

In the state of disallowed conformation (present structure), Tyr68 N forms a hydrogen bond with water molecule, W356 which in turn is hydrogen bonded to Thr67 O^{γ} and Gly11 O. On the other hand, in the structure of *Pa*Pth [29] where Tyr68 adopts an allowed conformation, Tyr68 N is not involved any interaction. Instead, the neighboring residue, Thr67 O forms a hydrogen bond with a corresponding water molecule, W262 which in turn forms two hydrogen bonds with Pro65 O and Gly11 O (Figure 6B). It is further seen that Tyr68 (present structure) is involved in a number of other interactions as it occupies an ith position in a segment, Tyr68 - Met69 - Asn70 - Arg71 which adopts a tight type 1 β-turn conformation. In this arrangement, Tyr68 O forms a hydrogen bond with Arg71 N at a distance of 3.02 Å. The corresponding hydrogen bond in *Pa*Pth [29] is 2.89 Å. Tyr68 O is also hydrogen bonded to Thr67 $O^{\gamma 1}$ at a distance of 2.85 Å. The corresponding hydrogen bond in *Pa*Pth [29] is 3.17 Å. The OH of the side chain of Tyr68 is linked to the side chain carboxylic group of Glu16 via a bridging water molecule, W332. The corresponding interaction in *Pa*Pth [29] is not observed because of disordering in the side chains of both Tyr68 and Glu16. The side chain of Tyr68 is flanked with the side chain of Pro13 to form van der Waals contacts. The similar interactions in *Pa*Pth [29] are weak due to the disordering in the side chain of Try68. Therefore, it may be concluded that the observed disallowed conformation of Tyr68 in Pth enzymes may be a preferred conformation. Thus the presence of a residue in the disallowed regions may not always be related to the quality of the structure but it may be a design of the structure for supporting the stability and function of proteins.

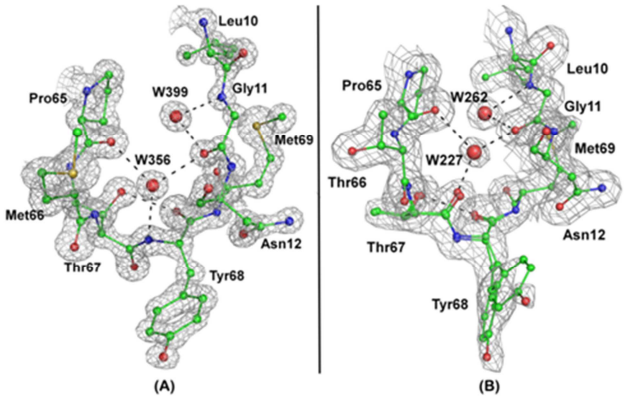

Figure 6. *(A). The conformation of Tyr68 was observed in the disallowed region of the Ramachandran's φ, ψ map in the present structure of AbPth. Similar conformations were observed in some other structures of Pth28, 30-31, 33, 36-37. (B.) The conformation of Tyr68 was observed in the allowed region of the Ramachandran's φ, ψ map in the structure of PaPth17. Similar conformations were observed in some other structures of Pth29, 32, 34-35.*

The backbone of *Ab*Pth adopts a β/α fold with seven β-strands and six α-helices, β1 (Ser5 - Leu10), α1 (Ala24 - Tyr36), β2 (Lys41 - Asp43), β3 (Gly48 - Arg52), β4 (His58 - Leu64), α2 (Ser72 - Phe82), β5 (Ala89 - Glu94), β6 (Val103 - Thr108), α3 (Leu118 - Ile125), β7 (His130 - Ile136), α4 (Ser146 - Gly151), α5 (Asn156 - Gln179) and α6 (Pro181 - Asn188) (Figure 7). The seven β-strands are bundled in to a twisted β-pleated sheet in the center of the molecule while six α-helices are arranged to surround the β-pleated sheet from all sides except the side of the substrate binding site. Overall, the structure of *Ab*Pth contains a highly ordered core with B-

factors ranging from 7.0Å^2 to 10.0Å^2 (Figure 8). The values of B-factors of the outer part of the structure vary from 11.0Å^2 to 20.0Å^2 (Figure 8). However, the values of B-factors of a segment, (Gly140 - His148) which belongs the flexible loop, (Gly137 - Ala153), are more than 33.0Å^2 (Figure 8).

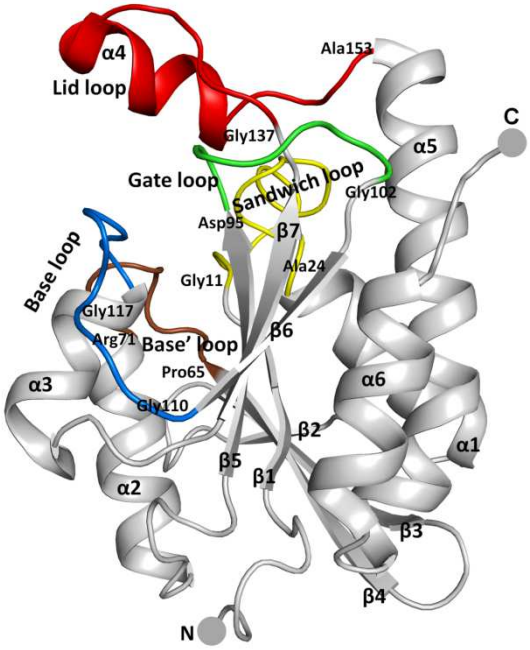

Figure 7. *Ribbon diagram of AbPth with secondary structure labels. N and C terminals are also indicated. Five loops, Gly11 - Ala24 (Sandwich loop, yellow), Pro65 - Arg71 (Base' loop, brown), Asp95 - Gly102 (Gate loop, green), Gly109 - Gly117 (Base loop, blue) and Gly137 - Ala153 (Lid loop, red) are also shown.*

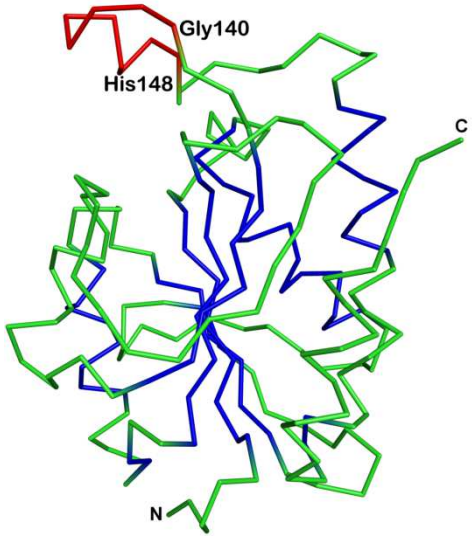

Figure 8. *The backbone tracing of AbPth indicating different ranges of B-factors. The blue colour corresponds to the values of B-factors in the range of 7.0 Å^2 to 10.0 Å^2. The green corresponds to a range of 11.0 Å^2 to 20.0 Å^2 while red is for above 33.0 Å^2.*

So far, structures of Pth from 12 different bacteria have been determined. There are seven structures from Gram-negative bacteria which include the current structure of *Ab*Pth and that of *Pa*Pth [29], *Ec*Pth [11], *St*Pth [30], *Bt*Pth [31], *Vc*Pth [32] and *Ft*Pth [33]. Four structures are from Gram-positive bacteria which include structures of *Ms*Pth [34], *Sa*Pth [35], *Tt*Pth [36] and *Sp*Pth [37]. The structure of *Mt*Pth [17] is also available. The r.m.s. deviations for the Cᵅ positions of *Ab*Pth, when superimposed on the structures of Pth enzymes from other Gram-negative bacteria, vary from 0.62Å to 0.83Å (Figure 9A). The r.m.s. deviations for the Cᵅ tracing of *Ab*Pth, when superimposed on the Cᵅ tracings of Pth enzymes from the Gram-positive bacteria, vary from 1.03Å to 1.48Å (Figure 9B) while the corresponding r.m.s. deviation when compared with *Mt*Pth is 1.24Å (Figure 9C). This shows that the structure of *Ab*Pth is more similar to the structures of Pth from Gram-negative bacteria than those from Gram-positive bacteria. The largest variations are observed in the conformations of a long loop, Gly137 - Ala153 which acts as a lid in Pth enzymes.

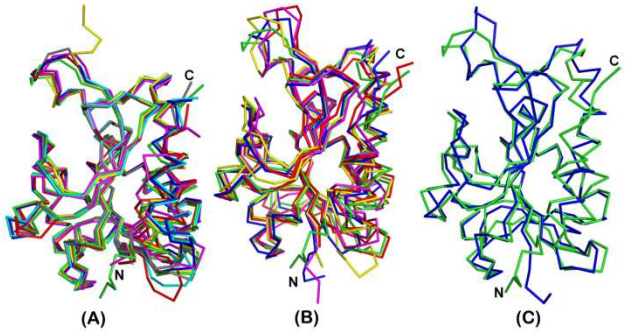

Figure 9. *Superimpositions of Cα traces of AbPth (green) on the Cα traces of Pth enzymes from (A) other Gram-negative bacteria including PaPth (red), EcPth (blue), StPth (cyan), BtPth (yellow), VcPth (grey) and FtPth (magenta). (B) Gram-positive bacteria including MsPth (magenta), SaPth(red), TtPth (blue) and SpPth (yellow) and (C) MtPth (blue). The largest variations are observed in the conformations of the Lid loop (Gly137 - Ala153).*

3.2. Water Structure in the Binding Site

The positions of a total of 239 water oxygen atoms have been determined. As seen from figure 10A, a novel arrangement of 18 water molecules, W329, W493, W416, W476, W488, W502, W336, W505, W393, W446, W378, W322, W461, W477, W492, W357, W444 and W405 has been observed. These water molecules are linked linearly through hydrogen bonds as W329---W493---W41---W476---W488---W502---W336---W505---W393---W446---W378---W322---W461---W477---W492---W357---W444---W405. Apart from the inter-water linear hydrogen bonds, there are 8 additional hydrogen bonds with amino acid residues, Asn70, Met69, Asn12, Asn116, Glu96, Asp98, His138 and Asn100. Starting point of this water chain is located at the mouth of the substrate binding site with W329 which is hydrogen bonded to Asn70 $O^{\delta 1}$. W416 forms three hydrogen bonds with Asn70 N, Asn70 $N^{\delta 2}$ and Met69 N. Another water molecule from the chain, W476 is hydrogen bonded to Asn12 $O^{\delta 1}$. W336 forms a hydrogen bond with Asn116 $N^{\delta 2}$ where as W446 is hydrogen bonded to Leu97 N. W378 forms two hydrogen bonds with Glu96 $O^{\varepsilon 1}$ and $O^{\varepsilon 2}$ while W477 is

hydrogen bonded to Arg133 N as well as to Asp98 $O^{\delta 1}$. W444 interacts with His138 N and the last water molecule in the chain, W405 forms a hydrogen bond with Asn100 $O^{\delta 1}$. As seen from figure 7B, the water chain begins from Asn70 on one side of the protein and ends at Asn100 which is located on the other side of the molecule (Figure 10B). The linear distance between the two ends from Asn70 $O^{\delta 1}$ to Asn100 $O^{\delta 1}$ is 26.0Å (Figure 10B). It may be of interest to note that the observed water chain runs across the catalytic site and separates the Lid loop from rest of the protein molecule. The two active site residues, His22 and Asp95 are inside of this chain while rest of the catalytically important residues such as Asn12, Asn70 and Asn116 are on the outside.

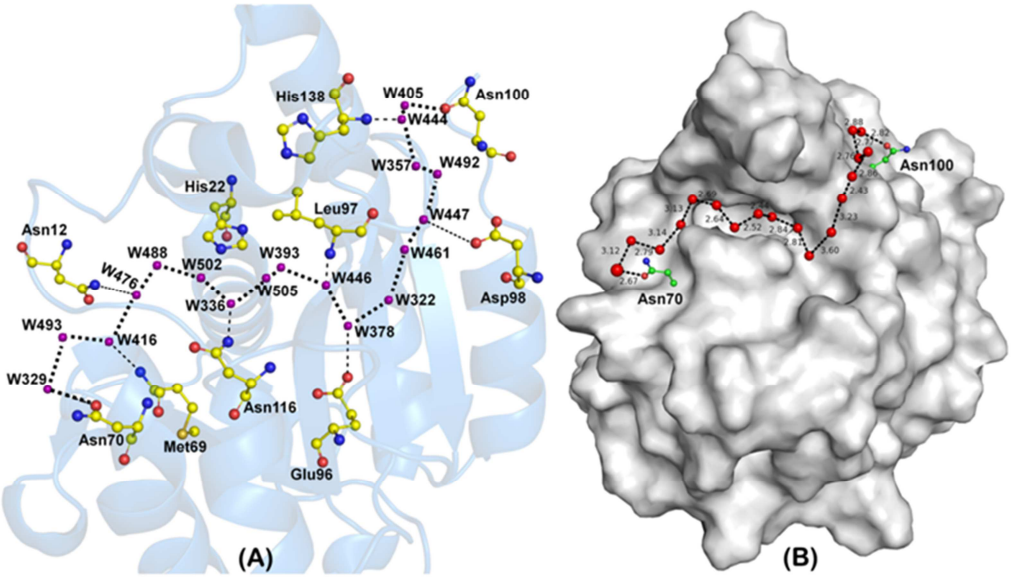

Figure 10. *(A) The hydrogen bonded linear chain of 18 water molecules. The amino acid residues which form hydrogen bonds with these water molecules are also shown. The dashed lines indicate hydrogen bonds (B). The positions 18 linearly hydrogen bonded water molecules are displayed in the GRASP representation of protein molecule. The residues, Asn70 and Asn100 are also shown.*

3.3. Structures of Active Site Loops

Previously, three loops were considered to discuss the flexibility in the structures of Pth enzymes [3, 28, 29, 36]. However, after a further critical examination of the active site region in Pth structures, two more loops related to active site region are included for critical analysis. In the further scheme of thing, five loops have been identified as (i) Sandwich loop, (Gly11 - Ala24) between β-strand, β1 and α-helix, α1, (ii) Base' loop, (Pro65 - Arg71) between β-strand, β4 and α-helix, α2, (iii) Gate loop, (Asp95 - Gly102) between β-strands, β5 and β6, (iv) Base loop, (Gly109 - Gly117) between β-strand, β6 and α-helix, α3, and (v) Lid loop, (Gly137 - Ala153) between β-strand, β7, and α-helix, α5 (Figure 7). The Sandwich loop is located between the Gate and Lid loops (Figure 7). This loop is anchored at two ends by β-strand, β1 and α-helix, α1. The first segment, Gly11 - Asn12 - Pro13 - Gly14 of this loop adopts an extended conformation while the next three overlapping segments, Ser15 - Glu16 - Tyr17 - Ala18, Tyr17 - Ala18 - Gln19 - Thr20 and Thr20 - Arg21 -His22 - Asn23 adopt tight β-turn conformations. The first segment forms a type 3 β-turn structure while the next two segments adopt type 1 β-turn conformations. The active site residue, His22 is part of the last tight type 1 β-turn structure. The Base' loop is tightly held at two ends by β-strand, β4 and α-helix, α2. The two segments Pro65 - Met66 - Thr67 and Tyr68 - Met69 - Asn70 - Arg71 are interconnected through a hydrogen bond, Thr67 O^{γ} --- Tyr68 O = 2.85Å. The second segment adopts a tight type 1 β-turn conformation. Asn70 of Base' loop plays an important role in the catalytic action. The Gate loop is held at two ends by two antiparallel β-strands, β5 and β6. The two segments, Glu96 - Leu97 - Asp98 - Met99 and Asn100 - Pro101 - Gly102 - Val103 of this loop adopt tight type 1 and type 2 β-turn conformations respectively. The Base loop is located at the bottom of the active site (Figure 7). The two overlapping segments in this loop, His112 - Gly113 - Gly114 - His115 and His115 - Asn116 - Gly117 - Leu118 adopt type 1' β-turn and type 3 β-turn conformations respectively. The overall structure of this loop is a highly ordered. Asn116 of this loop is involved in catalytic reaction. The Lid loop is a relatively long loop consisting of 17 amino acid residues. It is located on top of the active site (Figure 7). It has three distinct segments, (1) Gly137 - His138 - Pro139 - Gly140, (2) Ser141 - Lys142 - Gly143 - Arg144 and (3) Val145 - Ser146 - Gly147 - His 148 - Val149 - Leu150 - Gly151- Lys152 - Ala153. Segment (1) is a relatively flexible structure while segment (2) adopts a tight type 3 β-turn conformations while segment (3) consists of an α-helix, α4 for the subsegment, Ser146 - Gly151.

It is noteworthy that all the five loops have at least one segment with a tight β-turn structure indicating that the parts of these loops have relatively rigid structures. These loops are also interconnected through inter-loop hydrogen bonds including Asn12 $O^{\delta 1}$ --- Met69 N = 2.79Å (between Sandwich and Base' loops), His22 $N^{\varepsilon 2}$ --- Asn116 $N^{\varepsilon 2}$ =

2.77Å (between Sandwich and Base loops), Met99 O --- Gly137 N = 2.82Å (between Gate and Lid loops) and Asp95 $O^{\delta1}$ --- His115 $N^{\varepsilon2}$ = 2.82Å (between Gate and Base loops). It is noteworthy that the partners in these hydrogen bonds, generally, involve residues either from the beginning of the loops or from the ending stretches of the loops. The positions of these loops determine the overall stereochemical features of the substrate binding site including the plasticity of the active site region. The observed distances between loops in the structures of Pth from various bacteria may provide the information about their arrangements in the active site region. One such parameter pertains to comparing the distance between atoms Gly113 C^{α} (Base loop) and Asp98 $O^{\delta2}$ (Gate loop) which is estimated to be 8.25Å in the present structure of *Ab*Pth (Table 2). The corresponding distances in *Pa*Pth, *Ec*Pth, *St*Pth, *Bt*Pth, *Vc*Pth, *Ft*Pth, *Mt*Pth, *Ms*Pth, *Sa*Pth, *Tt*Pth and *Sp*Pth, were 6.08Å, 6.66Å, 5.74Å, 4.97Å, 6.60Å, 6.84Å, 3.33Å, 3.98Å, 6.56Å, 6.81Å and 8.78Å respectively (Table 2). Similarly, another distance between the Base and the Lid loops in the present structure of *Ab*Pth as measured between the atoms Gly113 C^{α} and Ser146 C^{α} was 13.47 Å while the corresponding distances in *Pa*Pth, *Ec*Pth, *St*Pth, *Bt*Pth, *Vc*Pth, *Ft*Pth, *Mt*Pth, *Ms*Pth, *Sa*Pth, *Tt*Pth and *Sp*Pth, were 13.25Å, 14.93Å, 14.37Å, 13.22Å, 13.54Å, 15.02Å, 11.41Å, 11.12Å, 15.29Å, 15.32Å and 13.02Å respectively (Table 2). Also the distance between the Base and Sandwich loops in the present structure of *Ab*Pth as measured between Gly113 C^{α} and His22 $C^{\varepsilon2}$ is 11.41Å while the corresponding distances in *Pa*Pth, *Ec*Pth, *St*Pth, *Bt*Pth, *Vc*Pth, *Ft*Pth, *Mt*Pth, *Ms*Pth, *Sa*Pth, *Tt*Pth and *Sp*Pth, were 10.09Å, 10.84Å, 10.24Å, 10.35Å, 10.37Å, 11.60Å, 9.41Å, 9.70Å, 11.17Å, 11.40Å and 10.38Å respectively (Table 2). Yet another distance of interest is between Asn70 C^{α} (Base' loop) and Asn116 C^{α} (Base loop) which is 5.11Å in *Ab*Pth while the corresponding values in *Pa*Pth, *Ec*Pth, *St*Pth, *Bt*Pth, *Vc*Pth, *Ft*Pth, *Mt*Pth, *Ms*Pth, *Sa*Pth, *Tt*Pth and *Sp*Pth were 5.24Å, 5.34Å, 5.40Å, 5.01Å, 4.69Å, 4.85Å, 5.49Å, 6.06Å, 5.17Å, 5.07Å and 5.11Å (Table 2). As seen from the above values, the distances of Gate, Lid and Sandwich loops from Base loop vary from 3.33Å to 8.78Å, 11.12Å to 15.32Å and 9.41Å to 11.40Å respectively while the distances between Asn70 Cα (Base' loop) and Asn116 Cα (Base loop) vary from 4.69Å to 6.06Å. These values indicate that the loops in the structures of Pth enzymes occupy significantly different positions. All the loops have one or more tight β-turns and also have one more intra-loop hydrogen bonds indicating the limited intra-loop flexibilities. The first four loops are loosely packed with each other in the active site region and may move significantly with respect to each other. On the other hand, the Lid loop represents a relatively longer segment (Gly137 - Ala153) and also protrudes out of the main body of the protein molecule. Because of its isolated position, it has a limited scope of grabbing interactions with other parts of the protein molecule. Thus the Lid loop can move more freely. It is noteworthy that the B-factors of atoms of the farthest segment in this loop, Gly140 - His148 have considerably higher values as compared to other parts of the loop. Also, the changes in the values of B-factors are abrupt. The B-factor of Pro139 is 17.5 $Å^2$ while the value for the next residue, Gly140, is 33.1 $Å^2$. Similarly, the B-factor for Val149 is 13.1 $Å^2$ while the value for the next residue, His148, is 59.2 $Å^2$. The values of B-factors for the rest of the residues, Ser141, Lys142, Glu143, Arg144, Val145, Ser146, Gly147 of the segment, Gly140 - His148 show narrow variations indicating a rigid body type movement from the hinge. This may allow the Lid loop to adopt open and close conformations.

A comparison of amino acid sequences of Pth enzymes from 12 different bacteria, whose structures are known, is shown in figure 2. The overall sequence identities of *Ab*Pth when compared with other Pth enzymes vary from 58% to 33%. The sequences identities of *Ab*Pth within the category of Gram-negative bacteria vary from 58% to 44% while the sequence identities of *Ab*Pth, when compared with those from Gram-positive bacteria, vary from 41% to 33%. It may be noted here that the residues involved in the catalytic process in *Ab*Pth are Asn12, His22, Asn70, Asp95 and Asn116. These residues are highly conserved in Pth enzymes of bacteria barring one exception in *Tt*Pth where Asn116 is replaced by Arg116 (Figure 2). It is also of interest to note that these five residues belong to four loops. The residues, Asn12 and His22 belong to loop, Gly11 - Ala24 while Asn70 is part of loop, Pro65 - Arg71 and residues, Asp95 and Asn116 are parts of loops, Asp95 - Gly102 and Gly109 - Gly117 respectively.

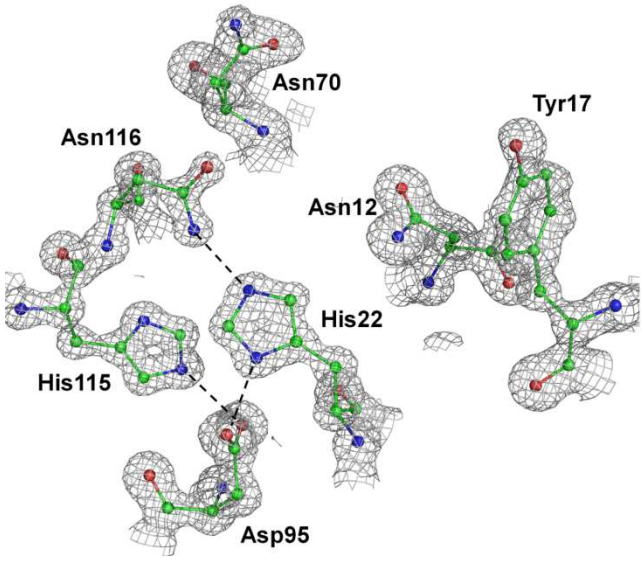

Figure 11. *The final (2Fo-Fc) electron density map at 1.5 σ cut off (black) for residues in the catalytic site. Hydrogen bonds are indicated by dashed lines.*

3.4. Catalytic Site

The residues involved in the catalytic activity in *Ab*Pth include Asn12, His22, Asn70, Asp95 and Asn116. The roles of Asn12, Asn70 and Asn116 have been described in earlier reports where Asn12 is said to be involved in the recognition of peptidyl-tRNA molecules while Asn70 and Asn116

participate in stabilizing the structures of catalytic intermediates [11, 36, 45-47]. As seen from final (2Fo-Fc) electron density map (Figure 11), the positions of all the non-hydrogen atoms in residues, Asn12, His22, Asn70, Asp95 and Asn116 were determined accurately. However, at this resolution, the electron density for the hydrogen atom in the catalytically important residue, His22 was not clearly observed. It may be mentioned here that three other structures of *Ab*Pth were also refined at 0.95Å (PDB ID, 6J93), 0.97Å (PDB ID, 6JJ1) and 0.99Å (PDB ID, 6JJQ) resolutions but these PDBs were not been used because of low completeness in the high resolution shells. Nevertheless, a difference Fourier (Fo - Fc) map computed using PDB ID, 6J93 has shown clear density at 2.5σ cut off for the hydrogen atom at $N^{\delta 1}$ of His22 (Figure 5) indicating that $N^{\delta 1}$ is protonated.

As seen from figure 9A, Asp95 $O^{\delta 2}$ forms a hydrogen bond with His22 $N^{\delta 1}$ at a distance of 2.62 Å while His22 $N^{\varepsilon 2}$ is hydrogen bonded to Asn116 $N^{\delta 2}$ at a distance of 2.77 Å. However, when a ligand is bound at the active site and interacts with His22, the side chain of Asn116 moves away considerably to interact with the bound ligand [28] (Figure 12B). In the native structure of *Ab*Pth, the torsion angle χ (N - C^{α} - C^{β} - C^{γ}) for Asn116 is 65º while the value of the corresponding torsion angle in the complex[28] is -75º. It shows that the side chain of Asn116 is present in a flexible environment as both conformations with χ values of around 60º [17, 34, 37] and -70º [11, 17, 29-36] are observed. In the complex, Asn12, Asn70 and Asn116 form hydrogen bonds with ligand (Figure 9B) thus indicating their roles in stabilizing the catalytic intermediates.

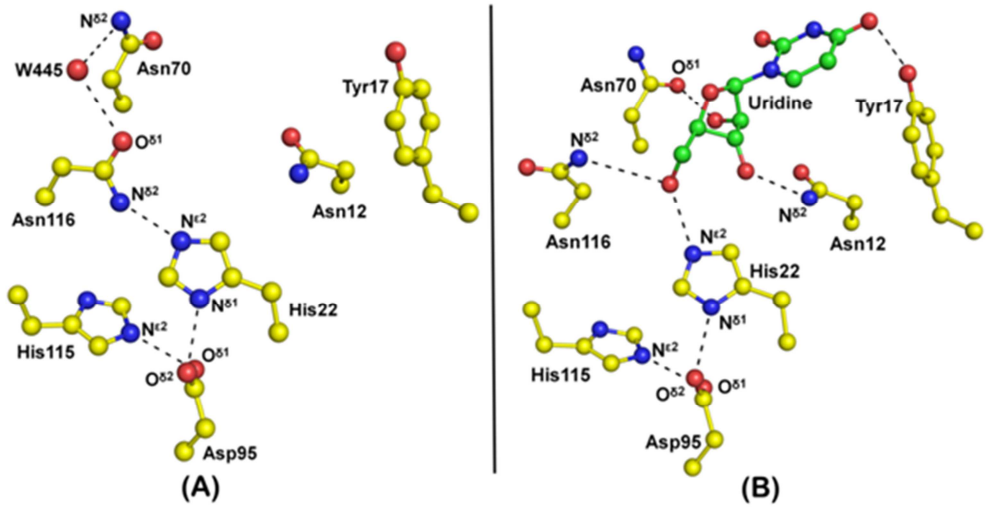

Figure 12. *(A) The interactions involving catalytic residues in AbPth are shown. The hydrogen bonds are indicated by dashed lines. Asp95 $O^{\delta}2$ forms a hydrogen bond with His22 $N^{\delta}1$ and His22 $N\varepsilon 2$ forms a hydrogen bond with Asn116 $N^{\delta}2$. (B) Catalytic residues in the structure of the complex of AbPth with uridine (PDB ID, 4JX9) are drawn. The hydrogen bonds are indicated by dashed lines. Asp95 $O^{\delta}2$ forms a hydrogen bond with His22 $N^{\delta}1$ and His22 $N\varepsilon 2$ forms a hydrogen bond with uridine instead of Asn116 $N^{\delta}2$.*

The stringent structural environment for a favorable stereochemical arrangement of His22 and Asp95 can be understood by examining the interactions of both His22 which acts as a catalytic base and Asp95 which controls the protonation state of His22. As seen from the structure of *Ab*Pth (Figure 7), His22 is a part of a well-ordered Sandwich loop which is held firmly between β-strand, β1 and α-helix, α1. Similarly, Asp95 is the first residue of a tightly formed Gate loop between two antiparallel β-strands, β5 and β6. It may also be noted here that the neighboring His115 is flanked on one side of His22 and Asp95 (Figure 12A). As seen from figure 12A, His115 $N^{\varepsilon 2}$ forms a hydrogen bond with Asp95 $O^{\delta 1}$ at distance of 2.82 Å while $N^{\delta 1}$ forms two hydrogen bonds with donor backbone nitrogen atoms of Gly117 and Leu118. On the other hand, Asn70 is aligned with Asn116 so that Asn116 attains a stereo chemically favorable disposition so that it can interact with His22 in the native state and move away to interact with the ligand upon complex formation (Figure 12B). On the other side, Val149 O forms a hydrogen bond with His22 N while the side chain of Val149 provides the stabilizing van der Waals contacts with other side chain atoms of His22. All these interactions contribute to create an overall favorable stereochemical arrangement of catalytic residues.

4. Conclusions

*Ab*Pth hydrolyzes the substrate, peptidyl-tRNA by cleaving the ester bond between the C-terminal carboxyl group of peptide and tRNA to generate the free tRNA and peptide molecules. The electron densities for hydrogen atoms in the rigid parts of the structure have been clearly observed. Although the electron densities for hydrogen atoms of residues in the active site region were not observed in the present structure but there were clear indications that $N^{\delta 1}$ of His22 (PDB ID, 6J93) was protonated. The hydrogen bond was formed between Asp95 $O^{\delta 2}$ and His22 $N^{\delta 1}$ while His22 $N^{\varepsilon 2}$ formed a hydrogen bond with Asn116$N^{\delta 1}$. This high resolution structure has also revealed that the side chains of several amino acid residues adopt multiple conformations.

The conformation of Tyr68 in the disallowed region is related to structural stability and functional requirement because Tyr68 is part of the substrate binding cleft. The observation of a chain of 18 linearly hydrogen bonded water molecules is novel. The conformations of Sandwich, Base', Gate and Base loops and their association in the active site region provided the structural basis of the understanding of plasticity in Pth enzymes. The large scale conformational flexibility of the Lid loop indicates the existence of both, the open and closed states. The structural differences between *Ab*Pth and other enzymes of Gram-negative bacteria are less pronounce than those observed between *Ab*pth and enzymes of Gram-positive bacteria.

Acknowledgements

Authors thank Indian Council of Medical Research, New Delhi for financial support. The grants from Science and Engineering Board (SERB) under the Distinguished Fellowship and National Post-doctoral Fellowship programs to TPS and VV are gratefully acknowledged and PKS thanks All India Institute of Medical Sciences, New Delhi for the grant of a fellowship.

References

[1] Manley JL. Synthesis and degradation of termination and premature-termination fragments of beta-galactosidase in vitro and in vivo. J Mol Biol 1978; 125: 407- 432.

[2] Jørgensen F, Kurland CG. Processivity errors of gene expression in Escherichia coli. J Mol Biol 1990; 215: 511-521.

[3] Singh NS, Varshney UA. Physiological connection between tRNA and peptidyl-tRNA hydrolase functions in Escherichia coli. Nucleic Acids Res 2004; 32: 6028 - 6037.

[4] Cruz-Vera LR, Magos-Castro MA, Zamora-Romo E, Guarneros G. Ribosome stalling and peptidyl-tRNA drop-off during translational delay at AGA codons. Nucleic Acids Res 2004; 32: 4462 - 4468.

[5] Menninger JR. Peptidyl transfer RNA dissociates during protein synthesis from ribosomes of Escherichia coli. J Biol Chem 1976; 251: 3392 – 3398.

[6] Atherly AG. Peptidyl-transfer RNA hydrolase prevents inhibition of protein synthesis initiation. Nature 1978; 275: 769.

[7] Menninger JR. Accumulation of peptidyl tRNA is lethal to Escherichia coli. J. Bacteriol 1979; 137: 694-696.

[8] Menez J, Heurgué-Hamard V, Buckingham RH. Sequestration of specific tRNA species cognate to the last sense codon of an overproduced gratuitous protein. Nucleic Acids Res 2000; 28: 4725-4732.

[9] Menninger JR, Walker C, Tan PF. Studies on the metabolic role of peptidyl-tRNA hydrolase. Properties of a mutant E. coli with temperature-sensitive peptidyl-tRNA hydrolase. Mol Gen Genet 1973; 121: 307-324.

[10] Shiloach J, Bauer S, de Groot N, Lapidot Y. The influence of the peptide chain length on the activity of peptidyl-tRNA hydrolase from E. coli. Nucleic Acids Res 1975; 2: 1941-1950.

[11] Schmitt E, Mechulam Y, Fromant M, Plateau P, Blanquet S. Crystal structure at 1.2 Å resolution and active site mapping of Escherichia coli peptidyl-tRNA hydrolase. EMBO J 1997; 16: 4760 – 4769.

[12] Jost JP, Bock RM. Enzymatic hydrolysis of N-substituted aminoacyl transfer ribonucleic acid in yeast. J Biol Chem 1969; 244: 5866 – 5873.

[13] Ouzounis C, Bork P, Casari G, Sander C. New protein functions in yeast chromosome VIII. Protein Sci 1995; 4: 2424 - 2428.

[14] Menez J, Buckingham RH, de Zamaroczy M, Campelli CK. Peptidyl-tRNA hydrolase in Bacillus subtilis, encoded by spoVC, is essential to vegetative growth, whereas the homologous enzyme in Saccharomyces cerevisiae is dispensable. Mol Microbiol 2002; 45: 123 -129.

[15] Rosas-Sandoval G, Ambrogelly A, Rinehart J, Wei D, Cruz-Vera LR, Graham DE, Stetter KO, Guarneros G, Söll D. Orthologs of a novel archaeal and of the bacterial peptidyl-tRNA hydrolase are nonessential in yeast. Proc Natl Acad Sci 2002; 99: 16707 – 16712.

[16] Fromant M, Schmitt E, Mechulam Y, Lazennec C, Plateau P. Blanquet S. Crystal structure at 1.8 A resolution and identification of active site residues of Sulfolobus solfataricus peptidyl-tRNA hydrolase. Biochemistry 2005; 44: 4294 – 30.

[17] Selvaraj M, Roy S, Singh NS, Sangeetha R, Varshney U, Vijayan M. Structural plasticity and enzyme action: crystal structures of mycobacterium tuberculosis peptidyl-tRNA hydrolase. J Mol Biol 2007; 372: 186-193.

[18] McShan WM, Ferretti JJ, Karasawa T, Suvorov AN, Lin S, Qin B, Jia H, Kenton S, Najar F, Wu H, Scott J, Roe BA, Savic DJ. Genome sequence of a nephritogenic and highly transformable M49 strain of *Streptococcus pyogenes.* J Bacteriol 2008; 190: 7773 - 7785.

[19] Dinçbas V, Heurgué-Hamard V, Buckingham RH, Karimi R, Ehrenberg M. Shutdown in protein synthesis due to the expression of mini-genes in bacteria. *J Mol Biol*. 1999; 291 (4): 745-759.

[20] Hughes RC, McFeeters H, Coates L, McFeeters RL. Recombinant production, crystallization and X-ray crystallographic structure determination of the peptidyl-tRNA hydrolase of Pseudomonas aeruginosa. Acta Crystallogr. Sect. F Struct. Biol. Cryst. Commun. 2012; 68: 1472-1476.

[21] Ito K, Murakami R, Mochizuki M, Qi H, Shimizu Y, Miura K, Ueda T, Uchiumi T. Structural basis for the substrate recognition and catalysis of peptidyl-tRNA hydrolase. Nucleic Acids Res 2012; 40: 10521-10531.

[22] Kossel H. Purification and properties of peptidyl-tRNA hydrolase from Escherichia coli. Biochim. Biophys Acta 1970; 204: 191- 200.

[23] Brun G, Paulin D, Yot P, Chapeville F. Peptidyl-tRNA hydrolase: demonstration in various organisms. Enzymatic activity in the presence of ribosomes. Biochimie 1971; 53: 225-231.

[24] Powers R, Powers R, Mirkovic N, Goldsmith-Fischman S, Acton TB, Chiang Y, Huang YJ, Ma L, Rajan PK, Cort JR, Kennedy MA, Liu J, Rost B, Honig B, Murray D, Montelione GT. Solution structure of Archaeglobus fulgidis peptidyl-tRNA hydrolase (Pth2) provides evidence for an extensive conserved family of Pth2 enzymes in archea, bacteria, and eukaryotes. Protein Sci 2005; 14: 2849-2861.

[25] Fromant M, Ferri-Fioni ML, Plateau P, Blanquet S. Peptidyl-tRNA hydrolase from Sulfolobus solfataricus. Nucleic Acids Res 2003; 31: 3227-3235.

[26] Dujeancourt L, Richte R, Chrzanowska-Lightowlers ZM, Bonnefoy N, Herberta CJ. Interactions between peptidyl tRNA hydrolase homologs and the ribosomal release factor Mrf1 in S. pombe mitochondria. Mitochondrion 2013; 13: 871-880.

[27] Atherly AG, Menninger JR. Mutant E. coli strain with temperature sensitive peptidyl-transfer RNA hydrolase. Nat New Biol 1972; 240: 245-246.

[28] Kaushik S, Singh N, Yamini S, Singh A, Sinha M, Arora A, Kaur P, Sharma S, Singh, T. P. The Mode of Inhibitor Binding to Peptidyl-tRNA Hydrolase: Binding Studies and Structure Determination of Unbound and Bound Peptidyl-tRNA Hydrolase from *Acinetobacter baumannii*. PLoS ONE 2013; 8: e67547.

[29] Singh A, Kumar A, Gautam L, Sharma P, Sinha M, Bhushan A, Kaur P, Sharma S, Arora A, Singh TP. Structural and binding studies of peptidyl-tRNA hydrolase from Pseudomonas aeruginosa provide a platform for the structure-based inhibitor design against peptidyl-tRNA hydrolase. Biochem J 2014; 463: 329-337.

[30] Vandavasi V, Taylor-Creel K, McFeeters RL, Coates L, McFeeters H. Recombinant production, crystallization and X-ray crystallographic structure determination of peptidyl-tRNA hydrolase from Salmonella typhimurium. Acta Crystallogr F Struct Biol Commun 2013; 70: 872-877.

[31] Baugh L, Gallagher LA, Patrapuvich R, Clifton MC, Gardberg AS, Edwards TE, Armour B, Begley DW, Dieterich SH, Dranow DM, Abendroth J, Fairman JW, Fox D, Staker BL, Phan I, Gillespie A, Choi R, Nakazawa-Hewitt S, Nguyen MT, Napuli A, Barrett L, Buchko GW, Stacy R, Myler P. J., Stewart LJ, Manoil C, Van Voorhis WC. Combining functional and structural genomics to sample the essential Burkholderia structome. PLoS One 2013; 8, e53851.

[32] Kabra A, Kabra A, Shahid S, Pal RK, Yadav R, Pulavarti SV, Jain A, Tripathi S, Arora A. Unraveling the stereochemical and dynamic aspects of the catalytic site of bacterial peptidyl-tRNA hydrolase. RNA 2017; 23: 202-216.

[33] Clarke TE, Romanov V, Lam R, Gothe SA, Peddi SR, Razumova EB, Lipman RSA, Branstrom AA, Chirgadze NY. Structure of Francisella tularensis peptidyl-tRNA hydrolase. Acta Crystallogr. Sect. F Struct. Biol. Cryst. Commun 2011; 67: 446-449.

[34] Kumar A, Singh N, Yadav R, et al. Crystal structure of peptidyl-tRNA hydrolase from mycobacterium smegmatis reveals novel features related to enzyme dynamics. Int J Biochem Mol Biol. 2012; 3: 58-69.

[35] Zhang F, Song Y, Niu L, Teng M, Li X. Crystal structure of Staphylococcus aureus peptidyl-tRNA hydrolase at a 2.25 Å resolution. Acta Biochim. Biophys 2015; 47, 1005-1010.

[36] Matsumoto A, Uehara Y, Shimizu Y, Ueda T, Uchiumi T, Ito K. High-resolution crystal structure of peptidyl-tRNA hydrolase from Thermus thermophilus. Proteins. 2019; 87: 226-235.

[37] Singh A, Gautam L, Sinha M, Bhushan A, Kaur P, Sharma S, Singh TP. Crystal structure of peptidyl-tRNA hydrolase from a Gram-positive bacterium, Streptococcus pyogenes at 2.19 Å resolution shows the closed structure of the substrate-binding cleft. FEBS Open Bio 2014; 4: 915-922.

[38] Kaushik S, Iqbal N, Singh N, et al. Search of multiple hot spots on the surface of peptidyl-tRNA hydrolase: structural, binding and antibacterial studies. Biochem J 2018; 475: 547-560.

[39] Kabsch W. XDS. Acta Crystallogr D Biol Crystallogr 2010; 66: 125–132.

[40] Matthews BW. Solvent Content of Protein Crystals. J Mol Biol 1968; 33: 491-496.

[41] Murshudov GN, Skubák P, Lebedev AA, Pannu NS, Steiner RA, Nicholls RA, Winn MD, Long F, Vagin AA. REFMAC5 for the refinement of macromolecular crystal structures. Acta Crystallogr D Biol Crystallogr 2011; 67: 355-367.

[42] Emsley P, Cowtan K. Coot: model-building tools for molecular graphics. Acta Crystallogr D Biol Crystallogr 2004; 60: 2126-2132.

[43] Laskowski RA, MacArthur MW, Moss DS, Thornton JM. PROCHECK: a program to check stereo chemical quality of protein structures. J Appl Crystallogr 1993; 26: 283-291.

[44] Ramachandran GN, Sasisekaran V. Conformation of polypeptides and proteins. Adv. Protein Chem 1968; 23: 283-438.

[45] Fromant M, Plateau P, Schmitt E, Mechulam Y, Blanquet S. Receptor site for the 50 -phosphate of elongator tRNAs governs substrate selection by peptidyl-tRNA hydrolase. Biochemistry 1999; 38: 4982-4987.

[46] Giorgi L, Plateau P, O'Mahony G, et al. NMR-based substrate analog docking to Escherichia coli peptidyl-tRNA hydrolase. J Mol Biol 2011; 412: 619-633.

[47] Goodall JJ, Chen GJ, Page MG. Essential role of histidine 20 in the catalytic mechanism of Escherichia coli peptidyl-tRNA hydrolase. Biochemistry 2004; 43: 4583-4591.

[48] DeLano WL. Pymol: An open-source molecular graphics tool. CCP4 Newsletter On Protein Crystallography. 2002; 40: 82-92.